



**HAL**  
open science

## **Influence of silicon content on the precipitation of secondary carbides and fatigue properties of a 5%Cr tempered martensitic steel**

Denis Delagnes, Pascal Lamesle, M. H. Mathon, N Mebarki, Christophe Levaillant

### ► To cite this version:

Denis Delagnes, Pascal Lamesle, M. H. Mathon, N Mebarki, Christophe Levaillant. Influence of silicon content on the precipitation of secondary carbides and fatigue properties of a 5%Cr tempered martensitic steel. *Materials Science and Engineering: A*, 2005, 394 (1-2), pp.435-444. 10.1016/j.msea.2004.11.050 . hal-01715084

**HAL Id: hal-01715084**

**<https://hal.science/hal-01715084>**

Submitted on 15 Mar 2019

**HAL** is a multi-disciplinary open access archive for the deposit and dissemination of scientific research documents, whether they are published or not. The documents may come from teaching and research institutions in France or abroad, or from public or private research centers.

L'archive ouverte pluridisciplinaire **HAL**, est destinée au dépôt et à la diffusion de documents scientifiques de niveau recherche, publiés ou non, émanant des établissements d'enseignement et de recherche français ou étrangers, des laboratoires publics ou privés.

# Influence of silicon content on the precipitation of secondary carbides and fatigue properties of a 5%Cr tempered martensitic steel

D. Delagnes<sup>a,b,\*</sup>, P. Lamesle<sup>a</sup>, M.H. Mathon<sup>c</sup>, N. Mebarki<sup>a,b</sup>, C. Levailant<sup>a</sup>

<sup>a</sup> Ecole des Mines d'Albi Carmaux, Campus Jarlard, Route de Teillet, F-81013  
Albi Cedex 09, France

<sup>b</sup> Centre d'Elaboration des Matériaux et d'Etudes Structurales, CNRS, 29 rue Jeanne Marvig, BP 94347,  
F-31055 Toulouse Cedex 4, France

<sup>c</sup> Laboratoire Léon Brillouin (CEA-CNRS), CEA Saclay, F-91191 Gif-sur-Yvette, France

## Abstract

In comparison with the conventional AISI H11 tool steel, which contains approximately 1 wt.% silicon, the modified steel AISI H11 (~0.35 wt.% silicon) exhibits improved tensile and fatigue properties at 550 °C – the estimated tool surface temperature during the high-pressure injection of aluminium alloys. The effect of silicon on the stability of secondary carbides was studied using transmission electron microscopy and small-angle neutron scattering. Silicon has a considerable influence on the precipitation of secondary carbides. A higher volume fraction and density of small particles were observed in the low-silicon-grade steel, both after heat treatment and after fatigue testing. The final discussion focuses on the influence of silicon in the precipitation sequence. It is concluded that silicon has a detrimental effect as it shifts the secondary hardening peak towards lower tempering temperatures.

*Keywords:* 5%Cr martensitic steel; Tempering; Secondary carbides; Isothermal fatigue; Silicon

## 1. Introduction

Martensitic steels containing 5%Cr were originally developed for the die casting of aluminium alloys. AISI H11 steel is probably one of the most widely used among all the existing hot work die steels. Other typical applications include forging dies, punches, mandrels, extrusion tools, etc. The main requirements after heat treatment are high strength and toughness to give a superior resistance to mechanical and thermal shocks and to the erosive action of molten aluminium [1]. Nevertheless, the fatigue resistance is not totally understood, as there is no clear correlation between fatigue and tensile properties. In fact, probably due to an unstable complex microstructure containing a high density of tangled dislocations

and secondary carbides, the slightest modification of composition or heat treatment can have a huge impact on mechanical properties. This latter fact underpins continued research activities and offers several ways of improving the mechanical resistance of tempered martensitic steels. One of the most well-known way is the modification of the concentration of alloying elements directly involved in the precipitation of secondary carbides, which shifts the secondary hardening peak towards higher temperatures. These alloying elements can be divided into two different categories depending on their effect on precipitation: (a) carbide forming elements such as Mo, V, W, Nb, etc. and (b) elements only modifying the tempering kinetics such as Co, Si, etc. The effect of silicon on the tempering behaviour of steels has been widely investigated since the outstanding work by Owen [2] 50 years ago. However, only limited information exists on alloyed steels tempered above the temperature of the secondary hardening

\* Corresponding author. Tel.: +33 5 63 493248; fax: +33 5 63 493099.  
E-mail address: delagnes@enstima.fr (D. Delagnes).

peak mainly induced by the intense precipitation of secondary carbides (hot work steels). The aim of the present work is to provide such information.

## 2. Experimental

### 2.1. Materials and heat treatment

The chemical compositions of the standard and the modified AISI H11 steels are shown in Table 1. The silicon content of the modified steel (called LS for low silicon) was strongly reduced in comparison with that of standard steel (called HS for high silicon). Heat treatment includes austenitising at 980 °C for 1 h followed by air cooling, a first tempering at 550 °C for 2 h and finally a second tempering for 2 h at 625 °C for the HS grade and at 623 °C for the LS grade. The hardness obtained after heat treatment is close to 42HRC for the two grades.

### 2.2. Microstructural investigations

The microstructure of the specimens was investigated by transmission electron microscopy (TEM) and X-ray diffraction (XRD). Observations were performed using JEOL 2010 and Philips CM12 microscopes. The latter is equipped with an energy-dispersive X-ray analyser (EDX). Carbides were extracted from the martensitic matrix using the well-known replica technique in order to avoid contribution from the matrix to the chemical analysis. First, specimens were cut to small parallelepipeds (4 mm × 2 mm × 2 mm) and one side was polished with silicon carbide paper down to 2400 grit. The polished surface was lightly etched with 5 vol.% nital for 8 s before the deposition of a carbon coating of nearly 35 nm onto the etched surface. An extraction replica was then prepared by electrolytic etching in a solution of 10 vol.% hydrochloric acid in ethanol until the carbon film was detached and, after washing, collected on grids.

Selected area diffraction and EDX were performed in order to determine crystal structure and chemical composition of the carbides. The distribution of carbide sizes was obtained from TEM micrographs for nearly 600 particles per specimen. In order to evaluate the total weight fraction of carbides, a dissolution technique of the martensitic matrix was used. Carbides were extracted by an electrolytic method described in [3]. Crystallographic structure and chemical composition analyses were performed using a Brucker

D5000 diffractometer equipped with a Cu K $\alpha$  radiation source and a graphite crystal monochromator and scintillation counter.

The neutron scattering experiments were performed at the Laboratoire Léon Brillouin (CEA-CNRS), Saclay, on the PAXE small-angle instrument. The wavelength  $\lambda$  was 0.6 nm and the sample-to-detector distance ( $D$ ) was 2 m, covering a scattering vector ( $q$ ) range from 0.3 to 1.6 nm $^{-1}$  ( $q = 4\pi \sin \theta / \lambda$ , where  $2\theta$  is the scattering angle). Measurements were performed at room temperature, under a saturating magnetic field of  $H = 2$  T perpendicular to the incident neutron beam direction, in order to separate the magnetic and nuclear scattering cross-sections.

The thickness ( $e$ ) of samples for small-angle neutron scattering (SANS) experiments, pre-cut and mechanically polished, is reduced between 0.5 and 1 mm. The measured transmission values ( $\cong 97\%$  for  $e = 0.5$  mm and  $\cong 90\%$  for  $e = 1$  mm) showed that multiple scattering corrections were unnecessary.

The measured intensities were corrected using the standard computer programs of the Laboratoire Léon Brillouin for sample transmission, background intensity as well as detector response [4]. The analysis method has been reported elsewhere [5].

In the case of ferromagnetic materials, the SANS intensity is the result of two contributions, nuclear and magnetic, which depend, respectively, on the difference in composition and in magnetisation between the particles and the matrix. In terms of cross-section, the SANS intensity can be written as

$$I(q) = \frac{1}{V_p} \frac{d\Sigma}{d\Omega}(q) = f_p [\Delta\rho_{\text{nucl}}^2 + \Delta\rho_{\text{mag}}^2 \sin^2 \alpha] \times F^2(q, R) S(q, R), \quad (1)$$

where  $I$  is the diffused intensity,  $V_p$  stands for the particle volume,  $d\Sigma/d\Omega$  the macroscopic differential cross-section,  $f_p$  the precipitated volume fraction, and  $F(q, R)$  the form factor of the particle.  $F(q, R)$  includes a size distribution function  $h(R)$ , which is taken here as two symmetric normalised Gaussian distributions. As the majority of small precipitates observed in TEM has a spherical shape (see the Section 3.2.1), the particle form factor  $F(q, R)$  for spherical particles with a radius  $R$  was used.  $S(q, R)$  is the structure factor of the monodisperse hard-sphere model describing the interparticle interference effect, which is not negligible for a precipitated fraction larger than 0.01. This is calculated analytically by Ashcroft and Lekner [6] from the Percus–Yevick equation.  $\Delta\rho_{\text{nucl, mag}}$  are the nuclear and magnetic contrast terms given by

$$\Delta\rho_{\text{nucl, mag}} = \frac{b_{\text{nucl, mag}}^p}{v_{\text{at}}^p} - \frac{b_{\text{nucl, mag}}^m}{v_{\text{at}}^m}, \quad (2)$$

where  $b$  is the nuclear or magnetic mean scattering length in the precipitates (p) or in the matrix (m), and  $v_{\text{at}}^{\text{p, m}}$  is the mean atomic volume either of the precipitates or the matrix.  $\alpha$  is

Table 1  
Chemical composition (wt.%) of the standard and the modified AISI H11 steels

	C	Mn	Si	Cr	Mo	V	Fe
Standard = HS	0.40	0.49	0.92	5.05	1.25	0.47	Balance
Modified = LS	0.36	0.36	0.35	5.06	1.25	0.49	Balance

the angle between the magnetisation of the sample and the scattering vector  $q$ .

As the magnetic moments lie parallel to the field  $H$ , the magnetic scattered intensity is zero in that direction and maximum in the normal direction. Consequently, the nuclear cross-section can be measured at  $\alpha = 0$ , while the sum of the nuclear and the magnetic cross-section is measured at  $\alpha = \pi/2$ . Subsequently, the magnetic contrast can be calculated by a simple subtraction. Some information about chemical composition can be deduced from the ratio between those two quantities, called  $A$ -ratio. For homogeneous particles, the  $A$ -ratio depends on the chemical composition, magnetisation and atomic density variations between precipitates and the matrix, and is given by

$$A = \frac{(d\Sigma/d\Omega)_{\perp\vec{H}}}{(d\Sigma/d\Omega)_{\parallel\vec{H}}} = \frac{\Delta\rho_{\text{nuc}}^2 + \Delta\rho_{\text{mag}}^2}{\Delta\rho_{\text{nuc}}^2} = 1 + \frac{\Delta\rho_{\text{mag}}^2}{\Delta\rho_{\text{nuc}}^2}. \quad (3)$$

The calculated  $A$ -ratio values for vanadium carbides (VC type) and chromium carbides ( $M_7C_3$  type) in the  $\alpha$ -Fe matrix are, respectively, equal to 2.2 and 3.4. Scattering lengths necessary to the calculation of the  $A$ -ratio were extracted from Ref. [7].

The relevant parameters obtained from the fitting of the relation (1) to the experimental data are:

- the factor  $J$  in the relation (1) independent of the size distribution and containing the fraction of particles:

$$J = f_p[\Delta\rho_{\text{nuc}}^2 + \Delta\rho_{\text{mag}}^2] \quad (4)$$

- the mean size of the particles (radius  $R$ );
- the full-width at the half-maximum of the Gaussian distribution.

An example of comparison between calculated and corrected experimental intensities as a function of  $q$  is shown in Fig. 1. In spite of the different hypotheses formulated to

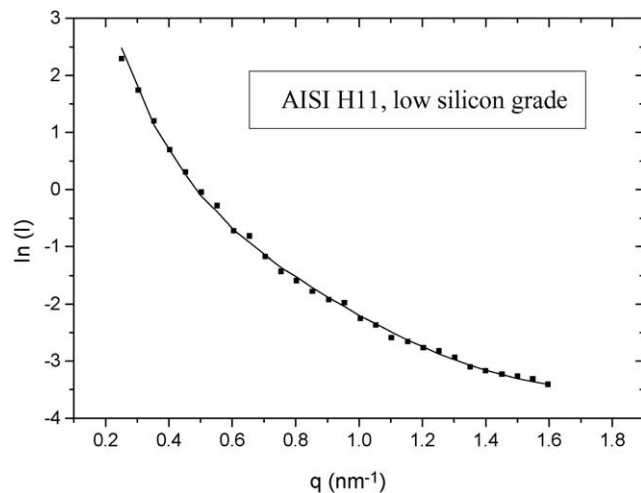


Fig. 1. Corrected intensities as a function of the scattering vector: comparison between measured data and the calculated curve according to Eq. (1).

calculate the corrected intensities, the fit of the relation (1) to the experimental data is reasonable for all the investigated specimens.

### 2.3. Isothermal fatigue testing

Total strain-controlled fatigue tests were carried out on a servohydraulic testing machine equipped with a resistance furnace. The axial strain was controlled and measured with a 10 mm gauge length extensometer. The waveform of the cycle was triangular at a frequency of 1 Hz, the mean strain being zero. Fatigue tests were performed at 550 °C, which is the surface tool temperature in high-pressure die casting operations [8], with total strain amplitudes lying between 0.7 and 2.0%. The specimen surface polishing was performed down to 1  $\mu$ m diamond suspension.

## 3. Results

### 3.1. Tensile and fatigue properties

The tensile properties obtained at 550 °C are shown in Table 2. Lowering the silicon content results in a noticeable increase in the 0.2% yield strength. This is an important mechanical parameter as the stress calculated on the tool surface is inferior or close to the 0.2% yield strength depending on the considered zone on the die. The other properties are slightly improved (see Table 2).

To compare the two steel grades, both fatigue behaviour and life duration were analysed. Concerning the cyclic loading, martensitic or bainitic steels have typical fatigue behaviour: an overall significant softening till rupture [9–20] as shown in Fig. 2. The stress amplitude versus number of cycles curve can be divided into two parts. A sharp softening is observed during the first few hundred cycles followed by a more gradual softening throughout the greater part of the lifetime. The dramatic decrease in the stress amplitude at the end of life is due to the propagation of one or several cracks in the specimen gauge length. The cyclic softening is first associated with a strong decrease of the dislocation density generated during the quench as particularly shown in [20] and a subsequent modification of the dislocation structure. The second mechanism involved in the softening is the coalescence of precipitates [21–24] which also modifies the free slip distances of dislocations.

Table 2  
Tensile properties obtained at 550 °C: comparison between the high silicon and low silicon grades

	0.2% yield strength (MPa)	Ultimate tensile strength (MPa)	Elongation at fracture (%)	Reduction in area (%)
HS	619	845	19.8	78
LS	675	854	22.6	81

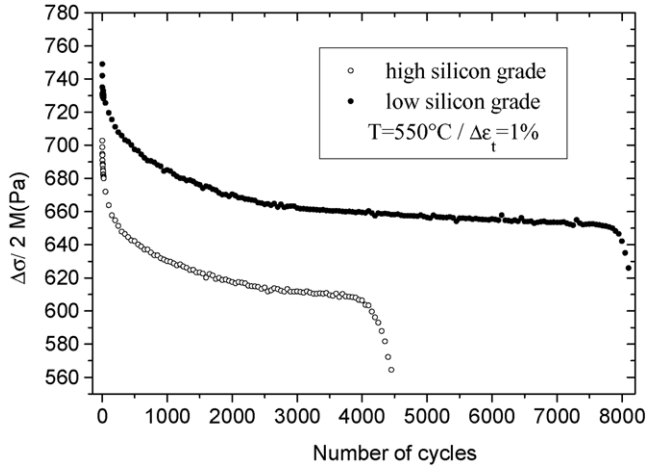


Fig. 2. Evolution of the stress amplitude according to the number of cycles showing the significant softening of martensitic steels ( $\Delta\varepsilon_t = 1\%$ ).

The softening amplitude,  $D$ , is defined by

$$D = \left(\frac{\Delta\sigma}{2}\right)_{N=1} - \left(\frac{\Delta\sigma}{2}\right)_{N=N_f/2}, \quad (5)$$

where  $N$  is the number of cycles,  $N_f$  the number of cycles to failure and  $\Delta\sigma/2$  the stress amplitude. Fig. 3 shows that there is no significant difference between the two grades.

Both the Manson-Coffin and Basquin laws rationalise the fatigue lifetime. When results are plotted in a Manson-Coffin diagram (see Eq. (6)), fatigue lifetimes of both grades are similar, as shown in Fig. 4 [21]. However, when the lifetime increases, the plastic strain amplitude tends to 0 and the measurement is not possible with a conventional extensometer:

$$\frac{\Delta\varepsilon_p}{2} = \varepsilon'_f (2N_f)^c, \quad (6)$$

where  $\Delta\varepsilon_p/2$  is the plastic strain amplitude measured at half-life,  $\varepsilon'_f$  the fatigue ductility coefficient and  $c$  the fatigue ductility exponent.

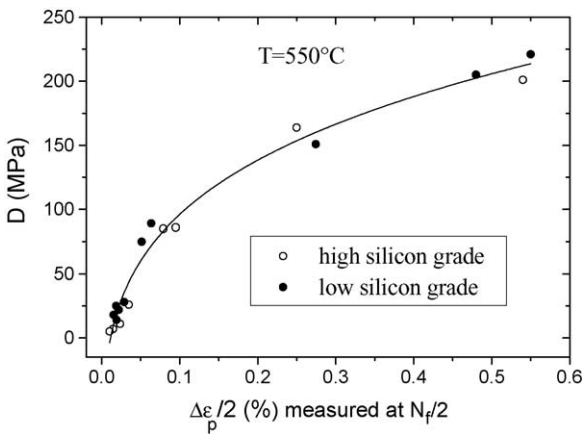


Fig. 3. Total softening amplitudes as a function of  $\Delta\varepsilon_p/2$  measured at  $N_f/2$ : comparison between the two grades.

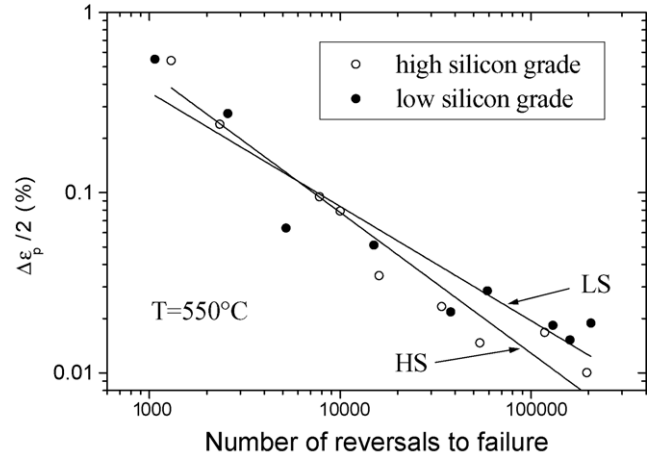


Fig. 4. Manson-Coffin plots obtained at  $550^\circ\text{C}$ .

The results of endurance tests are better expressed as a plot of the stress range measured at half-life:

$$\frac{\Delta\sigma}{2} = C(N_f)^p \quad (7)$$

where  $C$  and  $p$  are, respectively, the coefficient and the exponent of the Basquin law. When results are plotted in a Basquin diagram (see Fig. 5), the exponent  $p$  has the same value for the two grades and Basquin curves are parallel. Therefore, a lifetime ratio LR between the two grades, which is independent of the stress range, can be estimated by

$$\text{LR}_{\text{LS/HS}} = \left(\frac{C_{\text{HS}}}{C_{\text{LS}}}\right)^{1/p}. \quad (8)$$

Fatigue lifetimes of the LS grade are nearly five times higher than those of the HS grade. Consequently, lowering the silicon content in the AISI H11 steel results in increasing the fatigue lifetime at  $550^\circ\text{C}$ .

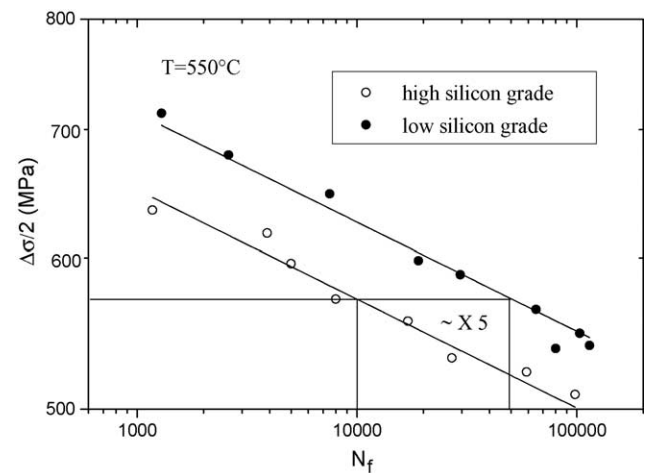


Fig. 5. Basquin plots obtained at  $550^\circ\text{C}$ .

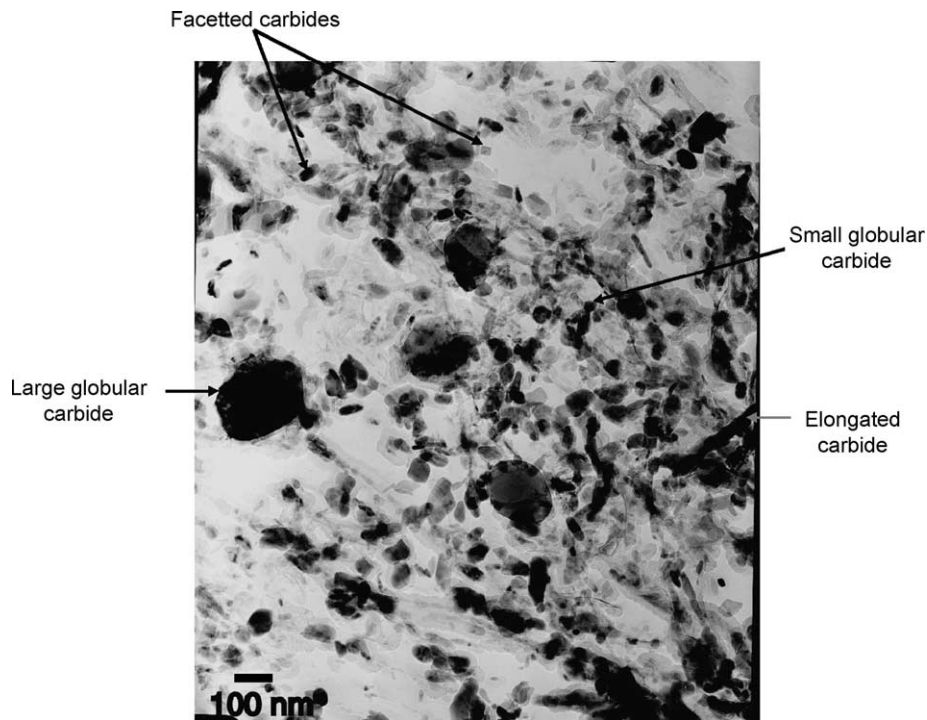


Fig. 6. Bright-field TEM image of the carbides extracted from the martensitic matrix (low silicon grade).

### 3.2. Secondary carbides

#### 3.2.1. Sequence of precipitation

After heat treatment, four types of carbides were identified by diffraction patterns and EDX depending on their morphology (see Fig. 6). No significant differences were observed between the two grades:

- (i) faceted carbides with a ratio length/width between 1 and 1.5: hexagonal CrFe carbides ( $M_7C_3$  type),
- (ii) large globular carbides (100–300 nm): face-centred cubic CrFe carbides ( $M_{23}C_6$  type),
- (iii) elongated carbides: orthorhombic FeCr carbides ( $M_3C$  type),
- (iv) small globular carbides (<40 nm): face-centred cubic V carbides (MC type).

M stands for metallic elements.

XRD complementary results, only obtained for the LS grade, allow the determination of the sequence of precipitation. Fig. 7 shows the evolution of carbide compositions according to the heat treatment. The results can be summarised as follows: as-annealed steel contains  $M_2C$  (M = Mo mainly),  $M_3C$  (M = Fe mainly),  $M_{23}C_6$  (M = Fe and Cr mainly) and a small fraction of MC (M = V mainly) carbides. After quenching, only the vanadium carbide (MC) and small quantities of  $M_3C$  and  $M_{23}C_6$ , probably not dissolved during the austenitisation were found. After the first and the second tempering, X-ray analysis has shown the presence of MC,  $M_3C$ ,  $M_7C_3$  and traces of  $M_{23}C_6$  carbides.

The TEM characterisation of carbides prior to, and after tempering, confirms the precipitation of MC,  $M_3C$  and  $M_7C_3$  carbides during tempering in both grades. Therefore, MC and  $M_7C_3$  are unambiguously the main carbides involved in the secondary hardening peak position and intensity visible on a diagram presenting tensile strength versus tempering temperature.

#### 3.2.2. Precipitation of secondary carbides after the second tempering

For both investigated grades, two different populations of secondary carbides were identified by TEM after tempering:

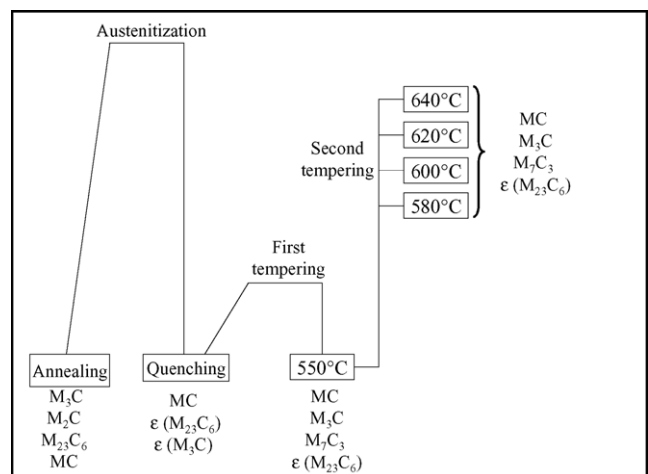


Fig. 7. Sequence of the precipitation of carbides.



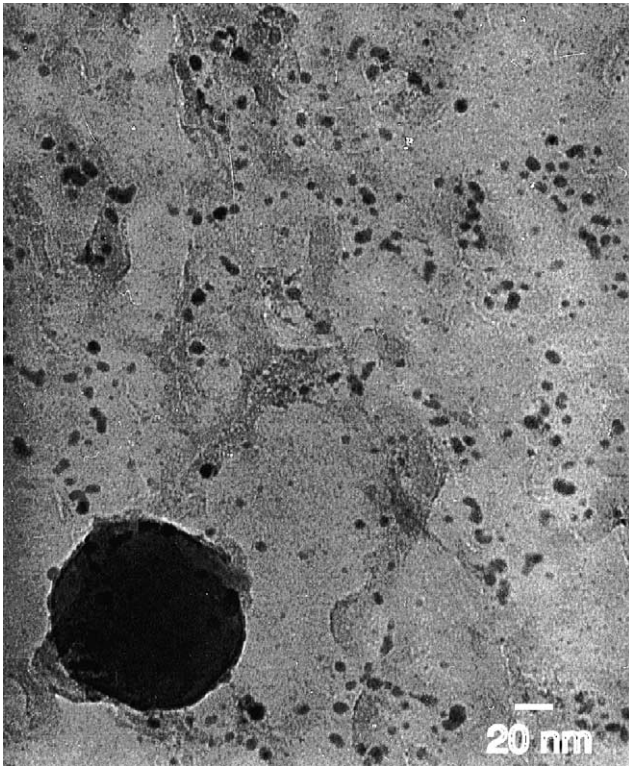


Fig. 8. Bright-field TEM image of the first population of carbides (note that the large carbide in the bottom left hand corner is a  $M_{23}C_6$  carbide not dissolved during the austenitisation; low silicon grade).

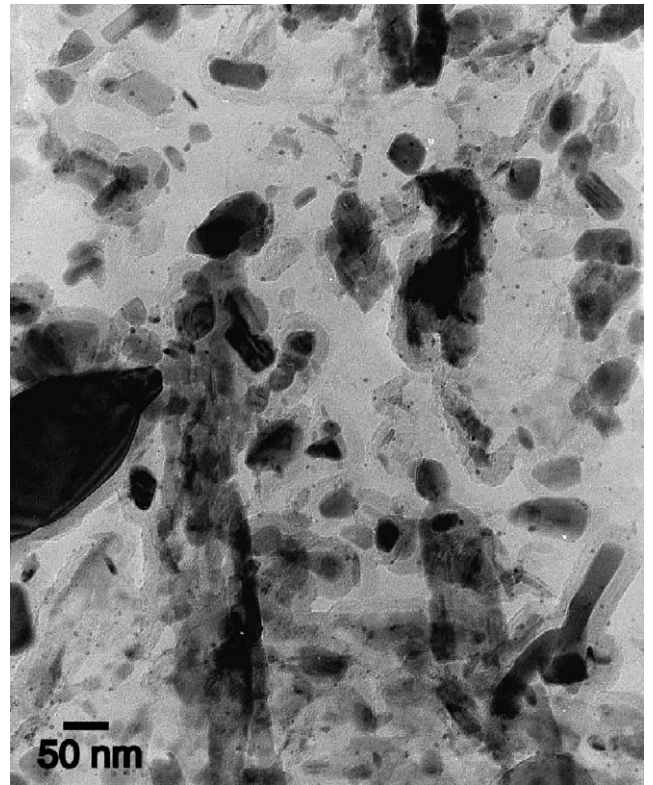


Fig. 9. Bright-field TEM image of the second population of carbides (low silicon grade).

- (i) small carbides with an average size close to 6 nm. This first population shown in Fig. 8 includes mainly vanadium carbides and a significantly smaller quantity of chromium carbides. However, the determination of the morphology was not possible with high enough accuracy for precipitates smaller than 5 nm;
- (ii) carbides with an average size in the range 20–40 nm as shown in Fig. 9. This second population includes both chromium and vanadium carbides and a few iron carbides.

Given a spherical shape, the size corresponds to the carbide diameter. For faceted or elongated carbides, the size is estimated by the addition of the apparent length and width divided by 2 (TEM observations on replicas).

The size distribution shown in Fig. 10 exhibits a bi-modal aspect. Clearly, the carbide quantity for the first population (smaller carbides) is significantly lower for the HS grade. Conversely, for the second population (larger carbides), the carbide quantity is much higher for the HS grade. In addition,

the average size of carbides including both populations is nearly 13 nm for the LS grade. This value should be compared with the mean size of 25 nm for the HS grade. The results obtained using SANS experiments are in good agreement with the main findings listed above (see the Table 3). The two populations were identified again. Nevertheless, the average size of the first population falls between 2 and 3 nm which is two or three times lower than the value obtained by TEM. This latter result is consistent with the fact that small carbides are probably not analysed by TEM and the distribution of size shown in Fig. 10 may largely deviate from the reality for the first three size intervals. In spite of the shape hypothesis (spherical instead of faceted carbides), the average size calculated by SANS is close to the estimation obtained by TEM for the second population.

The experimental value of the contrast ratio  $A$  as a function of the scattering vector is shown in Fig. 11. For large scattering vectors,  $A$  is very close to the value of 2.2 which corresponds to the theoretical value for the vanadium carbide VC. It means that small carbides are mainly vanadium carbides

Table 3

Comparison of the estimation of the average size of carbides obtained by SANS and by TEM ( $\sigma$  is the standard deviation of the Gaussian distribution)

	SANS		TEM	
	First population	Second population	First population	Second population
HS	2.6 nm/ $\sigma$ = 0.4 nm	33.5 nm/ $\sigma$ = 2.9 nm	6.1 nm/ $\sigma$ = 3.0 nm	28.8 nm/ $\sigma$ = 7.0 nm
LS	2.3 nm/ $\sigma$ = 0.5 nm	36.5 nm/ $\sigma$ = 2.8 nm	6.6 nm/ $\sigma$ = 2.7 nm	33.1 nm/ $\sigma$ = 5.7 nm

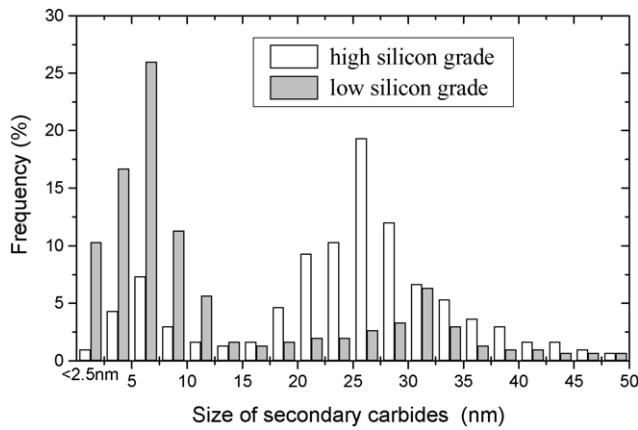


Fig. 10. Size distribution of secondary carbides: comparison between the high silicon and low silicon grades.

which is also consistent with EDX analysis. Assuming that the first population contains only the vanadium carbides, the volume fraction of the first population can be estimated using the relationship (4). The volume fraction derived for the LS and HS grades are, respectively, 0.58 and 0.31%. These values should, however, be compared with the total volume fraction estimated by the dissolution method which is nearly 6.5% for both grades. The total volume fraction includes the two populations, interlath iron carbides and  $M_{23}C_6$  carbides undissolved during austenitisation. However, only the first population is involved significantly in the strengthening mechanism as these fine intralath precipitates offer numerous pinning obstacles for the dislocations generated by quenching, thus preventing a quick rearrangement of the tangled dislocations. Consequently, the higher strengthening observed for the LS grade can be explained by a higher volume fraction of small intralath precipitates.

### 3.2.3. Influence of fatigue loading at 550 °C

Hot work die steels are generally simultaneously submitted to both elevated temperature and cyclic stress during ser-

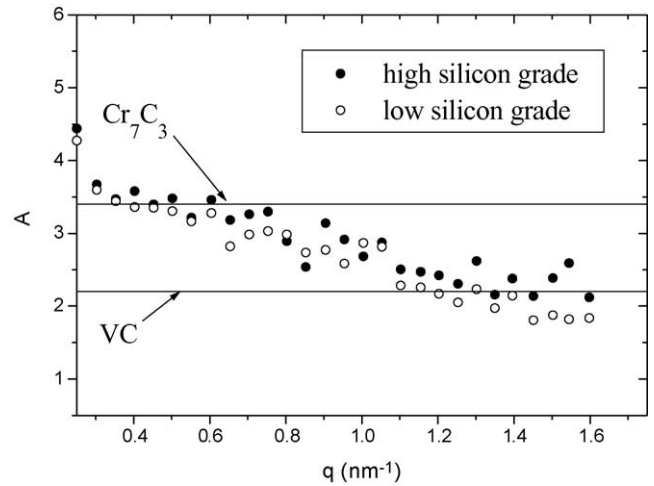


Fig. 11. Experimental contrast ratio  $A$  vs.  $q$ : comparison with the theoretical values calculated for VC and  $Cr_7C_3$  carbides.

vice. It is therefore relevant to investigate to what extent microstructural parameters are influenced by cyclic mechanical loading. TEM observations and SANS experiments were performed after a cyclic test at 550 °C with a total strain amplitude of 0.8 and 2%. Results are presented in Tables 4 and 5.

As shown in Table 5, an increase of the average size of carbides after a fatigue test is observed for both grades. As the duration of a fatigue test is quite short (less than 1 h for  $\Delta\varepsilon_t = 2.0\%$  including the heating time before starting the test) and as the testing temperature is 70 °C below the tempering temperature, it can be concluded that coalescence is only induced by fatigue. Indeed, a third tempering treatment in the same time and temperature conditions as the fatigue test has no effect on the mechanical properties. Such dynamic ageing has already been observed in other tempered martensitic steels [22–25]. Two different mechanisms can explain the enhanced carbide coalescence during fatigue. The driving force for the dynamic coalescence of carbides is the mechanical energy that complements the thermal energy, which, on

Table 4  
Estimation of the average size of carbides after a fatigue test at 550 °C

		SANS				TEM			
		First population		Second population		First population		Second population	
		$\Delta\varepsilon_t = 0.8\%$	$\Delta\varepsilon_t = 2\%$	$\Delta\varepsilon_t = 0.8\%$	$\Delta\varepsilon_t = 2\%$	$\Delta\varepsilon_t = 0.8\%$	$\Delta\varepsilon_t = 2\%$	$\Delta\varepsilon_t = 0.8\%$	$\Delta\varepsilon_t = 2\%$
Carbide size (nm)	HS	1.9 (0.4)	1.8 (0.4)	31.7 (2.6)	31.1 (3.1)	Not observed		33.5 (8.5)	36.5 (9.6)
	LS	2.3 (0.6)	2.1 (0.6)	30.8 (2.6)	31.6 (2.7)	8.1 (3.6)	10.7 (3.3)	34.9 (9.1)	33.1 (8.2)

$\sigma$  is the standard deviation of the Gaussian distribution and its values are given in parentheses.

Table 5  
Influence of a fatigue test performed at 550 °C on the average size of carbides and the volume fraction of the small carbides

		As heat-treated	After fatigue $\Delta\varepsilon_t = 0.8\%$	After fatigue $\Delta\varepsilon_t = 2\%$
Average size of carbides (nm)	HS	25.0	33.5	36.5
	LS	13.0	21.4	24.1
Volume fraction (%) of the 1st carbides population	HS	0.31	0.18	0.06
	LS	0.58	0.36	0.41



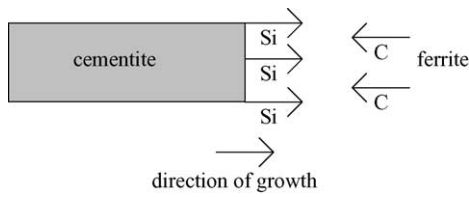


Fig. 12. Carbon and silicon flux during the coarsening of the cementite.

its own, is not sufficient to provide coalescence. The second mechanism is associated with pipe diffusion along dislocations, which is strongly affected by high-temperature plasticity. This kinetic effect was precisely described by Eggeler [22] for creep conditions.

The differences between the LC and HC grades after fatigue are summarised as follows:

- TEM observations show an increase in the average size of small carbides for the LS grade, whereas small carbides are no more found in the HS grade (see Table 4).
- The fatigue test induces a decrease of the volume fraction of small carbides estimated by the relation (4). This effect is stronger for the HS grade (Table 5).

In conclusion, results indicate that secondary carbides coalescence is clearly accelerated under fatigue at elevated temperature for both grades. After fatigue, a higher quantity of small carbides is revealed in the LS grade which is consistent with a better fatigue resistance.

#### 4. Discussion: influence of silicon on the precipitation

Silicon in normal concentrations is not a carbide-forming element in tool steels. However, it is already well known that silicon inhibits the precipitation of cementite. As one of the mechanism of nucleation of alloy carbides is the in situ nucleation at pre-existing cementite particles (i.e. the nuclei are formed on the interfaces between cementite and ferrite and the carbon is provided by the cementite), the precipitation of chromium and vanadium carbides is strongly influenced by the cementite stability during the first tempering.

Considering a cementite platelet in a Widmanstätten array during the first tempering as shown in Fig. 12, the coarsening is strongly dependent on carbon diffusion from the supersaturated ferrite towards cementite. As silicon has a very low solubility in cementite, silicon segregates at the interface carbide/supersaturated ferrite. Several authors [26–28] have performed chemical analysis close to cementite precipitates showing the high concentration of silicon rejected from the carbide in ferritic, bainitic and martensitic steels. Consequently, there is a silicon flux in the opposite direction to that of carbon (see Fig. 12).

The silicon and carbon concentrations as a function of the distance from the interface are shown in Fig. 13. During the growth of the cementite, the silicon concentration gradient is negative near the interface as the silicon is rejected from the

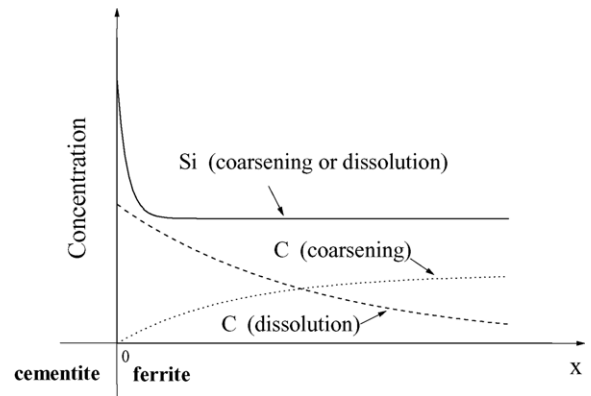


Fig. 13. Concentrations of carbon and silicon near the cementite/ferrite interface during the cementite coarsening and dissolution.

cementite. Conversely, the carbon concentration gradient is positive as the excess of carbon in the supersaturated ferrite allows the coarsening of the cementite. The kinetics is different as carbon (interstitial) diffuses much faster than silicon (substitutional). If the influences of all the alloying elements except silicon are neglected (i.e. a ternary alloy Fe–Si–C is considered), the carbon concentration gradient driving the growth of cementite is given by Fick's first law:

$$J_C = -D_{CC}^{\alpha\text{-Fe}} \frac{\partial C_C}{\partial x} - D_{CSi}^{\alpha\text{-Fe}} \frac{\partial C_{Si}}{\partial x}, \quad (9)$$

where  $D_{CSi}^{\alpha\text{-Fe}}$  is the cross-diffusion coefficient [29].

The influence of silicon on the tempering characteristics of low-alloyed steels has been extensively studied [2,26–28,30–36]. Even if discussions are still open [37], it is well established that silicon significantly delays the softening process of low-alloyed steels during tempering. There is considerable accumulated evidence that silicon reduces the flux of carbon required for the growth of cementite. This effect increases the strength of the steel at a fixed temperature since carbon remains in interstitial solid solution in the martensitic lattice or enables higher tempering temperatures to be used without severe loss in tensile strength. Consequently, the repulsive interaction between carbon and silicon in the martensite bulk results in a positive cross-diffusion coefficient in Eq. (9). The situation is therefore similar to that observed in austenite as originally shown by Darken [38]. The subsequent mathematical framework for the diffusion in multicomponent metallic solid solution was developed by Kirkaldy [39]. Due to experimental difficulties, thermodynamic data are not available for supersaturated ferrite. In addition, there is very little information on the influence of silicon on the tempering process at higher temperatures in steels containing sufficient carbide-forming elements to induce a secondary hardening peak above 500 °C.

Depending on the nucleation mechanism of alloyed carbides, the influence of silicon is summarised as follows:

- (i) For in situ nucleation at pre-existing cementite particles, carbon is provided by the adjacent cementite which

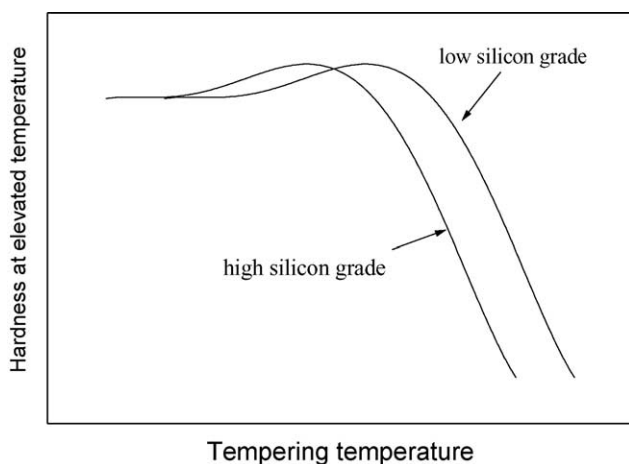


Fig. 14. Qualitative influence of silicon content on the secondary hardening peak.

gradually dissolves. Fig. 13 shows the carbon and silicon concentrations as a function of the distance from the interface during the cementite dissolution. According to Fick's first law and since  $D_{\text{CSi}}^{\alpha\text{-Fe}} > 0$ , the silicon gradient near the interface induces an increase of the flux of carbon in the  $x > 0$  direction accelerating the dissolution of cementite. Subsequent intensive precipitation of alloy carbides occurs and the secondary hardening peak tends to be shifted towards lower temperatures.

- (ii) For separate nucleation within the martensitic matrix, the effect of silicon is a delay in the coarsening of  $\text{Fe}_3\text{C}$  to such an extent that more carbon is available to form a finer carbide dispersion at lower temperatures just as in the previous case (i).

Consequently, the main benefits of the silicon addition seen in low-alloyed steels with high tensile strength [30,32] are obviously no longer observed in hot-work tool steels as the secondary hardening peak is shifted towards lower tempering temperatures. As the second tempering is generally performed above the temperature corresponding to the maximum hardening peak (see Fig. 14), an over-ageing for the HS grade may result in a lower tensile and fatigue strength which is consistent with the near total dissolution of the small carbides mentioned in the previous part.

## 5. Summary

The effects of silicon on fatigue resistance as well as carbides precipitation and coalescence have been investigated in two 5% chromium tool steel grades. TEM observations and SANS experiments were performed in order to analyse the variation in the average size and volume fraction of carbides after a double tempering and a fatigue test. The main differences between the standard AISI H11 steel containing nearly

1 wt.% silicon and the low silicon grade containing 0.35 wt.% silicon are summarised as follows:

- (i) Higher tensile and fatigue properties at 550 °C were observed in the low silicon grade.
- (ii) These differences are explained by a higher volume fraction of small secondary carbides (mainly vanadium carbides) in the low silicon grade.
- (iii) As silicon inhibits the coarsening of the cementite and promotes its dissolution, carbon is available to form alloy carbides at lower tempering temperatures for the high silicon grade. As a consequence, the secondary hardening peak of the low silicon grade is shifted towards higher temperatures.
- (iv) Reducing the silicon content in steels tempered above the secondary hardening peak results in a possible use of the tool in higher in-service temperatures (between 20 and 30 °C for the AISI H11 steel).

## Acknowledgements

The authors gratefully acknowledge the Aubert&Duval Holding (ADh) company for providing samples and financial support. Special thanks are given to Mr. A. Grellier, Mr. P.E. Richey and Mrs. M.F. Gervais from ADh for fruitful discussions. The authors also wish to thank Dr. C. Daffos from Ecole des Mines d'Albi-Carmaux (EMAC) for the precious help in the realisation and analysis of SANS experiments and Mr T. Gilroy from EMAC for the English improvement of the paper.

## References

- [1] G.A. Roberts, R.A. Cary, Tool Steels, 4th ed., American Society for Metals, Metals Park, OH, 1980.
- [2] W.S. Owen, Trans. ASM 46 (1954) 812.
- [3] C. Kim, V. Biss, W.F. Hosford, Metall. Trans. A 13 (1982) 185.
- [4] J.P. Cotton, in: P. Lindner, Th. Zemb (Eds.), Neutron X-ray and Light Scattering: Introduction for an Investigated Tool for Colloidal and Polymeric System, North-Holland Delta Series, Amsterdam, 1991, p. 19.
- [5] M.H. Mathon, A. Barbu, F. Dunstetter, F. Maury, N. Lorenzelli, C.H. de Novion, J. Nucl. Mater. 245 (1997) 224.
- [6] N.W. Ashcroft, J. Lekner, Phys. Rev. 145 (1966) 83.
- [7] V.F. Sears, Neutron News 3 (1992) 26.
- [8] G. Dour, M. Dargusch, C. Davidson, A. Nef, D. St John, in: A. Dahle (Ed.), Proceedings of the Conference Light Metals Technology, Brisbane, 2003, p. 155.
- [9] R.A. Fournelle, E.A. Grey, M.E. Fine, Metall. Trans. A 7 (1976) 669.
- [10] K. Kanazawa, K. Yamaguchi, K. Kobayashi, Mater. Sci. Eng. 40 (1979) 89.
- [11] F. Martin, J. Petit, J. de Fouquet, Mater. Sci. Eng. 61 (1983) 237.
- [12] J.B. Vogt, G. Degallaix, J. Foct, Fat Fract. Eng. Mater. Struct. 11 (1988) 435.
- [13] J.C. Earthman, G. Eggeler, B. Ilschner, Mater. Sci. Eng. A 110 (1989) 103.

- [14] S.R. Mediratta, V. Ramaswamy, V. Singh, R. Rao, *Steel Res.* 61 (1990) 325.
- [15] J.H. Beatty, G.J. Shifflet, *Metall. Trans. A* 22 (1991) 675.
- [16] H.J. Christ, C. Sommer, H. Mughrabi, A.P. Voskamp, J.M. Beswick, F. Hengerer, *Fat Fract. Eng. Mater. Struct.* 15 (1992) 855.
- [17] J.B. Vogt, S. Argillier, J. Leon, J.P. Massoud, V. Prunier, *ISIJ Int.* 39 (1999) 1198.
- [18] Z. Zhang, D. Delagnes, G. Bernhart, *Int. J. Fatigue* 24 (2002) 635.
- [19] S. Sankaran, V. Subramanya Sarma, K.A. Padmanabhan, *Mater. Sci. Eng. A* 345 (2003) 328.
- [20] J. Pesicka, R. Kuzel, A. Dronhofer, G. Eggeler, *Acta Mater.* 51 (2003) 4847.
- [21] D. Delagnes, Ph.D. Thesis, Ecole Nationale Supérieure des Mines de Paris, March 1998 (in French).
- [22] G. Eggeler, *Acta Metall.* 37 (1989) 3225.
- [23] H.J. Chang, C.H. Tsai, J.J. Kai, *Int. J. Pres. Ves. Piping* 59 (1994) 31.
- [24] Z.G. Wang, K. Rahka, P. Nenonen, C. Laird, *Acta Metall.* 33 (1985) 2129.
- [25] A. Joarder, N.S. Cheruvu, D.S. Sarma, *Mater. Charact.* 28 (1992) 121.
- [26] R.C. Thomson, M.K. Miller, *Appl. Surf. Sci.* 88–89 (1995) 185.
- [27] S.J. Barnard, G.D.W. Smith, A.J. Garratt-Reed, J. Vandersande, in: *The Metals Society (Eds.), Proceedings of the International Conference on Advances in the Physical Metallurgy and Applications of Steels*, Liverpool, London, 1981, p. 33.
- [28] T. Tarui, T. Takahashi, S. Ohashi, R. Uemori, *Iron Steelmaker* 21 (1994) 25.
- [29] A.G. Guy, V. Leroy, T.B. Lindemer, *ASM Trans.* 59 (1966) 517.
- [30] C.J. Altstetter, M. Cohen, B.L. Averbach, *ASM Trans.* 55 (1962) 287.
- [31] R.M. Hobbs, G.W. Lorimer, N. Ridley, *J. Iron Steel Inst.* 210 (1972) 757.
- [32] C.H. Shih, B.L. Averbach, M. Cohen, *ASM Trans.* 48 (1958) 86.
- [33] J. Gordine, I. Codd, *J. Iron Steel Inst.* 207 (1969) 461.
- [34] H.K.D.H. Bhadeshia, *Bainite in Steels*, Institute of Materials, London, 1992.
- [35] H.K.D.H. Bhadeshia, J.W. Christian, *Metall. Trans. A* 21 (1990) 767.
- [36] R.W.K. Honeycombe, H.K.D.H. Bhadeshia, *Steels: Microstructure and Properties*, 2nd ed., Edward Arnold Publishers Ltd., London, 1995.
- [37] N. Fujita, Ph.D. Thesis, University of Cambridge, February 2000.
- [38] L.S. Darken, *Trans. Am. Inst. Min. Met. Eng.* 180 (1949) 430.
- [39] J.S. Kirkaldy, *Can. J. Phys.* 35 (1957) 435.